JOURNAL OF GEOPHYSICAL RESEARCH, VOL. 114, C02024, doi:10.1029/2008JC005072, 2009

Estimates of bottom flows and bottom boundary layer dissipation of the oceanic general circulation from global high-resolution models

Brian K. Arbic,[1,2] Jay F. Shriver,[3] Patrick J. Hogan,[3] Harley E. Hurlburt,[3] Julie L. McClean,[4] E. Joseph Metzger,[3] Robert B. Scott,[1] Ayon Sen,[1,5,6] Ole Martin Smedstad,[7] and Alan J. Wallcraft[3]

Received 7 August 2008; revised 5 November 2008; accepted 30 December 2008; published 27 February 2009.

[1] This paper (1) compares the bottom flows of three existing high-resolution global simulations of the oceanic general circulation to near-bottom flows in a current meter database and (2) estimates, from the simulations, the global energy dissipation rate of the general circulation by quadratic bottom boundary layer drag. The study utilizes a data-assimilative run of the Naval Research Laboratory Layered Ocean Model (NLOM), a nonassimilative run of NLOM, and a nonassimilative run of the Parallel Ocean Program z-level ocean model. Generally speaking, the simulations have some difficulty matching the flows in individual current meter records. However, averages of model values of $|\mathbf{u}_b|^3$ (the time average of the cube of bottom velocity, which is proportional to the dissipation rate) computed over all the current meter sites agree to within a factor of 2.7 or better with averages computed from the current meters, at least in certain depth ranges. The models therefore likely provide reasonable order-of-magnitude estimates of areally integrated dissipation by bottom drag. Global dissipation rates range from 0.14 to 0.65 TW, suggesting that bottom drag represents a substantial sink of the ~1 TW wind-power transformed into geostrophic motions.

Citation: Arbic, B. K., J. F. Shriver, P. J. Hogan, H. E. Hurlburt, J. L. McClean, E. J. Metzger, R. B. Scott, A. Sen, O. M. Smedstad, and A. J. Wallcraft (2009), Estimates of bottom flows and bottom boundary layer dissipation of the oceanic general circulation from global high-resolution models, *J. Geophys. Res.*, *114*, C02024, doi:10.1029/2008JC005072.

1. Introduction

[2] The first goal of this paper is to compare the bottom flows in high-resolution ocean general circulation models to flows in near-bottom moored current meters. Because of improvements in computer power, bathymetric products, surface forcing products, numerical schemes, and subgrid-scale parameterizations, the realism of high-resolution ocean models has continued to improve in recent years. Though some comparisons of high-resolution models to data have focused on the full water column [e.g., *Penduff et al.*, 2006], most such comparisons have focused on the surface and upper ocean [e.g., *McClean et al.*, 2002; *Maltrud and McClean*, 2005]. Here we conduct a comprehensive comparison of bottom flows in global models with those observed in current meters.

[3] The emphasis on bottom flows is motivated by the second goal of the paper, which is to estimate, from the models, the energy dissipation rate of the oceanic general circulation by bottom boundary layer drag. In recent years considerable effort has been expended in quantifying the sources and sinks of mechanical energy for the oceanic general circulation [e.g., *Munk and Wunsch*, 1998; *Wunsch and Ferrari*, 2004]. One important energy source is the ~0.85–1 TW wind-power input transformed into geostrophic flows [e.g., *Wunsch*, 1998; *Scott*, 1999; *Huang et al.*, 2006; *Scott and Xu*, 2008]. How this energy input ultimately dissipates is not well understood. *Ferrari and Wunsch* [2008] can be consulted for a detailed overview. Candidate dissipation mechanisms include internal wave generation and breaking instigated by geostrophic flows over rough topography [e.g., *Naveira-Garabato et al.*, 2004; *Marshall and Naveira-Garabato*, 2008; *Nikurashin*, 2008] and energy transfer from geostrophic motions into internal waves and other submesoscale motions in the upper ocean [e.g., *Müller et al.*, 2005; *Polzin*, 2008]. Another candidate mechanism is bottom boundary layer drag. We

[1] Institute for Geophysics, Jackson School of Geosciences, University of Texas at Austin, Austin, Texas, USA.
[2] Now at Department of Oceanography and Center for Ocean-Atmospheric Prediction Studies, Florida State University, Tallahassee, Florida, USA.
[3] Oceanography Division, Naval Research Laboratory, Stennis Space Center, Mississippi, USA.
[4] Scripps Institution of Oceanography, University of California, San Diego, La Jolla, California, USA.
[5] Westwood High School, Austin, Texas, USA.
[6] Now at Department of Applied and Computational Math, California Institute of Technology, Pasadena, California, USA.
[7] Planning Systems, Inc., Stennis Space Center, Mississippi, USA.

0148-0227/09/2008JC005072$09.00

will focus on this mechanism here, though we do not discount the potential importance of the other mechanisms.

[4] Several lines of research point to the importance of bottom boundary layer drag for the dynamics and energy budget of the oceanic general circulation and its associated mesoscale eddy field. *Weatherly* [1984] estimated energy dissipation rates in bottom boundary layers for the Gulf Stream region, and found that they may balance nearly all of the local wind-power input. A series of papers [*Arbic and Flierl*, 2003, 2004; *Arbic et al.*, 2007; *Arbic and Scott*, 2008] have focused on the sensitivity of idealized geostrophic turbulence models to bottom drag, and argued that the horizontal scales, vertical structure, and amplitude of the modeled eddy kinetic energy compare well to those in observations only when bottom drag is moderately strong. This is true for both linear and quadratic bottom drag [*Arbic and Scott*, 2008]. Other studies [e.g., *Thompson and Schmitz*, 1989, and references therein; *Smith et al.*, 2002; *Riviere et al.*, 2004; *Cessi et al.*, 2006; *Thompson and Young*, 2006, 2007] have also found a significant sensitivity of ocean general circulation models and geostrophic turbulence models to the strength of bottom drag. Further motivation for the importance of bottom boundary layer drag comes from studies of the ocean tides. About 2/3 of the globally integrated tidal dissipation takes place in shallow seas, where tidal flows are exceptionally strong, primarily by bottom boundary layer drag [*Egbert and Ray*, 2003, and references therein].

[5] *Sen et al.* [2008] estimated the global energy dissipation rate of oceanic low-frequency flows by quadratic bottom boundary layer drag (hereafter, often referred to simply as the "dissipation rate") using observations alone. The dissipation estimates ranged from 0.21 to 0.83 TW (in waters deeper than 3000 m), a substantial fraction of the wind-power input. The dissipation was concentrated in regions of strong currents such as the Gulf Stream, consistent with the regional analysis of *Weatherly* [1984]. *Sen et al.* [2008] utilized a database of moored near-bottom current meters. Relationships computed at the mooring sites between surface flows measured by satellite altimetry and bottom flows measured by current meters were exploited to infer global maps of bottom flows from the global satellite measurements of surface flows. Here we compute the dissipation rate from direct estimates of bottom flow, taken from the high-resolution models.

[6] We use models with differing horizontal resolutions, vertical resolutions, and vertical coordinate formulations. We examine both data-assimilative and nonassimilative simulations of the Naval Research Laboratory Layered Ocean Model (NLOM) [*Shriver et al.*, 2007], as well as a nonassimilative simulation of the Parallel Ocean Program (POP) [*Maltrud and McClean*, 2005]. Both of the NLOM simulations are run at 1/32° horizontal resolution, while POP is run at 1/10° horizontal resolution. The greater horizontal resolution of the NLOM simulations is potentially an important advantage for the modeling of bottom flows. *Hurlburt and Hogan* [2000] and *Hogan and Hurlburt* [2000] showed that the abyssal eddy kinetic energy in 1/32° North Atlantic and Japan/East Sea regional simulations of NLOM was little different from that in 1/64° simulations. However, in 1/16° runs, abyssal eddy kinetic energy was noticably lower, and in 1/8° runs it was much lower. Thus at least in NLOM, 1/32° resolution is required to achieve convergence for abyssal eddy kinetic energy. (See *Wallcraft et al.* [2005] for a study of the numerical convergence of NLOM with respect to values of the eddy viscosity.) Consistent with these NLOM results, *Penduff et al.* [2006] showed that the abyssal eddy kinetic energies in 1/6° simulations of the CLIPPER model of the Atlantic Ocean were substantially weaker than those recorded by current meters. On the other hand, POP has greater vertical resolution than NLOM (40 z-levels versus 6 Lagrangian layers), and a more standard treatment of bottom topography (full-cell topography in a z-level model). As described in section 2.3, the topography used in NLOM is compressed in a somewhat nonstandard way. Vertical resolution and the treatment of topography thus represent an important potential advantage for POP.

[7] Prior to undertaking our analysis on a global scale, we will analyze the North Atlantic sectors of the three global models. The density of near-bottom current meters we can compare our models to is higher in the North Atlantic than in other regions. Furthermore, in a North Atlantic analysis we can include a fourth high-resolution simulation, the North Atlantic POP run of *Smith et al.* [2000]. As noted by *Maltrud and McClean* [2005], North Atlantic POP simulates the Gulf Stream more accurately than does global POP. As we will see, North Atlantic POP compares more closely to individual current meter records than the other three simulations, and thus serves as a useful point of comparison.

[8] We reiterate that this paper utilizes the output, such as it is, of existing high-resolution global simulations. We do not undertake new simulations for this paper, as such simulations are extremely expensive computationally. The ideal model output for an analysis such as ours with a focus on low-frequency motions would consist of either very frequently sampled (for instance, hourly) output, from which high-frequency motions can be removed with a low-pass filter, or temporal averages, i.e., daily averages. Hourly sampling of the models is not possible, at least for all model variables and all grid points in the vertical and horizontal directions, because of the unfeasibly large storage and analysis computers that this would require. The model output we use here consists of "snapshots" rather than temporal averages, meaning that there will be some aliasing of high-frequency motions into our analyses [*Jayne and Tokmakian*, 1997]. Later we will examine the impact on our results of the relatively infrequent temporal sampling of the NLOM and POP simulations.

[9] We will not endeavor to compute complete energy budgets of these models, as this would be extremely time-consuming given the vast size of the model outputs. Energy budgets of NLOM have been computed over limited regions, and with only two Lagrangian layers in the vertical direction. In these smaller computations it was found that the energy inputs and outputs did indeed balance well, with eddy viscosity and bottom drag together accounting for all of the dissipation [*Hurlburt and Thompson*, 1982; *Hurlburt*, 1986; *Schmitz and Thompson*, 1993]. Here we will simply compute the bottom drag dissipation term, by inserting the bottom flows from models into standard formulae for the dissipation rate. We will compute the wind-power input for one of the simulations (nonassimilative NLOM), to test

whether it is comparable to the inputs computed from observations in other studies.

[10] While the wind-power input is specifically calculated as an energy source for geostrophic motions, the bottom flows in both current meter data and high-resolution models are not strictly geostrophic. Current meter data can be filtered in the time domain to remove high-frequency ageostrophic motions such as inertial motions and tides. What remains has a strong overlap with geostrophic motions. For example, *Wunsch* [1997] found a good visual correspondence between maps of surface geostrophic motions computed from satellite altimetry and the surface extrapolation of low-frequency motions computed via current meters. Thus *Sen et al.* [2008] argued that it is meaningful to compare the ~1 TW power input transformed into geostrophic flows with the dissipation of low-frequency flows. Later we will show that the abyssal flows in nonassimilative NLOM, at least, are predominantly low frequency.

2. Ocean Models

2.1. North Atlantic POP

[11] We analyze year 1999 of the North Atlantic POP simulation of *Smith et al.* [2000]. This simulation has 40 z-levels in the vertical direction. The model output is saved as snapshots every 10 days. The horizontal grid for the output that we analyzed (downloaded from http://www.earthsystemgrid.org) ranges from 19.9°S to 72.6°N in the north–south direction, and from 98°W to 17.2°E in the east–west direction. Our North Atlantic analysis, of North Atlantic POP and of the North Atlantic sectors of the three global models, will be performed over this North Atlantic POP domain. The longitudinal bounds of this domain exclude the Gulf of Mexico. In North Atlantic POP, the Gulf of Mexico is inserted into Africa as a reentrant feature. However, since the global models are not run in this way, for simplicity we omit the Gulf of Mexico from the North Atlantic analysis of all four models. The latitudinal spacing of North Atlantic POP is 1/10° at the equator, and Mercator elsewhere, reducing to about 0.03° at high latitudes. The longitudinal spacing is 1/10° everywhere. Every vertical level of the North Atlantic POP output has 1280 by 992 grid points (in the north–south and east–west directions, respectively).

[12] As described by *Smith et al.* [2000], bottom topography for the North Atlantic POP simulation was derived from the 1/12° ETOPO5 database [*National Oceanographic and Atmospheric Administration NOAA*, 1986]. Following interpolation of this data set to the 1/10° Mercator grid, the depth at each horizontal grid point was set equal to that of the nearest vertical level in the model. Minor modifications were then made at the Straits of Florida, Faroe Bank Channel, and Strait of Gibraltar. The wind stress was derived from the 6 hourly ECMWF TOGA Global Surface Analysis, and then linearly interpolated to each model time step to avoid excitation of spurious inertial oscillations [*Jayne and Tokmakian*, 1997]. (Note that this temporal interpolation was done for the global POP and NLOM simulations as well). Other details of the surface forcing, e.g., surface heat and freshwater fluxes, and temperature and salinity restoration at the model horizontal boundaries, are described by *Smith et al.* [2000].

2.2. Global POP

[13] We analyze year 2003 of a global POP simulation, an extension of the multiyear simulation described at length by *Maltrud and McClean* [2005]. Our global POP analysis is also based on snapshots put out every 10 days. Global POP employs a displaced pole grid in the Northern Hemisphere to allow inclusion of the Arctic Ocean. The horizontal grid spacing of global POP is 1/10° at the equator. In the southern hemisphere, the grid is Mercator, while the northern hemisphere grid is smoothly distorted to allow for the displaced pole. The logical dimension of one level of global POP is 2400 by 3600.

[14] *Maltrud and McClean* [2005] should be consulted for full details of the model bathymetry and forcing fields, but we repeat a small portion of that discussion here. Nonpolar, Arctic, and Southern Ocean bathymetry was derived from *Smith and Sandwell* [1997], *Jakobsson et al.* [2000] (International Bathymetric Chart of the Arctic Ocean), and *Lythe and Vaughan* [2001] (BEDMAP), respectively. Again full cell topography was used, and again the model depth field was hand-modified in regions of important sills and channels such as the Canadian and Indonesian archipelagos, Denmark and Faroe-Shetland overflows, etc. Surface fluxes were calculated using a combination of the NCEP/NCAR reanalysis products [*Kalnay et al.*, 1996], as well as monthly data from various sources listed by *Maltrud and McClean* [2005]. Wind stress was calculated offline using the formulation of *Large and Pond* [1982] with climatological sea surface temperature taken from *Shea et al.* [1990]. Temperature and salinity distributions were generated using a combination of the Navy's 1/8° climatological product [*Fox et al.*, 2002] and the *Steele et al.* [2001] data set for the Arctic. Subsurface restoring was used in limited areas around some locations having overflows which are difficult to simulate (i.e., the Mediterranean Sea, Red Sea, and Persian Gulf).

2.3. Global NLOM

[15] We use 1 full year of output from a global data-assimilative NLOM simulation (denoted by DANLOM here) (in current use as a U.S. Navy operational model [*Shriver et al.*, 2007]) and 1 year of output from a global nonassimilative simulation (denoted by NANLOM here). As described by *Shriver et al.* [2007], DANLOM assimilates sea surface height from satellite altimeters and sea surface temperature from multichannel satellite infrared radiometers. The horizontal resolution of the NLOM simulations is 1/32° in latitude (ranging from 72°S to 65°N, for a total of 4384 grid points in the north–south direction) and 45/1024° in longitude (for a total of 8192 grid points in the east–west direction). Note that 1/32° NLOM has essentially twice as many grid points in each horizontal direction as does 1/10° global POP. The output we require from DANLOM and NANLOM (bottom velocities) was not saved over concurrent years. Thus we analyze DANLOM output from calendar year 2006 and NANLOM output from 2002. Snapshots of DANLOM output were saved daily, while NANLOM snapshots were saved every 3 days.

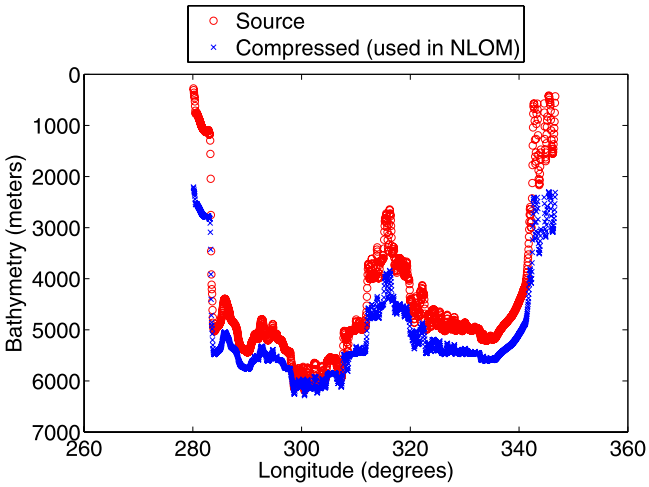

Figure 1. Illustration of the topography compression used in NLOM (see text). Bathymetry shown is along 28°N in the Atlantic. The source topography is taken from ETOPO5, with minimum and maximum depths set at 200 and 6500 m, respectively. The compressed topography is the topography actually used in NLOM.

[16] NLOM has Lagrangian layers in the vertical direction, and is based on the primitive equation model of *Hurlburt and Thompson* [1980], but with greatly expanded capability [*Wallcraft et al.*, 2003]. It has 6 dynamical layers and a bulk mixed layer. The source topography is a modified version of the 1/12° ETOPO5 data set [*NOAA*, 1986]. The maximum allowable depth of NLOM is set to 6500 m. The topography is vertically compressed to confine it to the lowest layer of NLOM. This is done by multiplying the height of the topography above the 6500 m reference level by a factor of 0.69. Confining the topography to the lowest layer avoids the problem of running a Lagrangian layer model with vanishingly thin layers. A solution to this problem exists [e.g., *Hallberg and Rhines*, 1996], but has not been implemented in NLOM. The lack of vanishingly thin layers in NLOM makes for greater computational efficiency, allowing it to be run at horizontal resolutions not yet feasible in other ocean models. NLOM has lateral boundaries that follow the 200 m isobath with a few exceptions, such as the shallow straits around the Japan/East Sea. Additional details are provided by *Shriver et al.* [2007, and references therein]. Figure 1 demonstrates the topography compression used in NLOM. Differences between the topography actually used in NLOM and the source topography are largest in shallow waters. The minimum depth of 200 m in the source topography yields a minimum depth in NLOM of 2153 m. As we will see later, the large differences between the source depths and the depths used in NLOM in shallow regions yield flows in these regions that are weaker than those in observations.

[17] The NLOM simulations were forced with a hybrid of the Fleet Numerical Meteorology and Oceanography Center (FNMOC) Navy Operational Global Atmospheric Prediction System (NOGAPS) [*Rosmond et al.*, 2002] and the *Hellerman and Rosenstein* [1983] wind stresses. The long-term mean (August 1990 to July 1999 for FNMOC) is subtracted from the FNMOC stresses and replaced by the annual mean from the *Hellerman and Rosenstein* [1983] data set.

3. Current Meter Data

[18] As in the paper by *Sen et al.* [2008], we use moored current meter data obtained from the Deep Water Archive and Buoy Group Archive of Oregon State University's Buoy Group (http://cmdac.oce.orst.edu/cds.html, or http://cmrecords.net). Since bottom boundary layer depths are of order 10 m [*Weatherly and Martin*, 1978], we require the current meters to lie at least 10 m above the sea bottom. We define a current meter as sufficiently near the seafloor if it is less than 10% of the seafloor depth above the seafloor. When multiple instruments from the same mooring fit our criteria, only the deepest instrument is used. Tides and other high-frequency motions are removed with a 72-hour low-pass filter. In records that contain data gaps, the filter is applied separately to each segment of complete data. Only current meter records exceeding 180 days in length are retained. Typical lengths of the current meter records we use range from 0.5–2 years. While the current meter database spans many years (1970s to present), the model output we analyze is confined to specific years, listed in section 2.

[19] We select only those mooring locations for which a model/data comparison involving all three global simulations can be made. The number of current meters in the

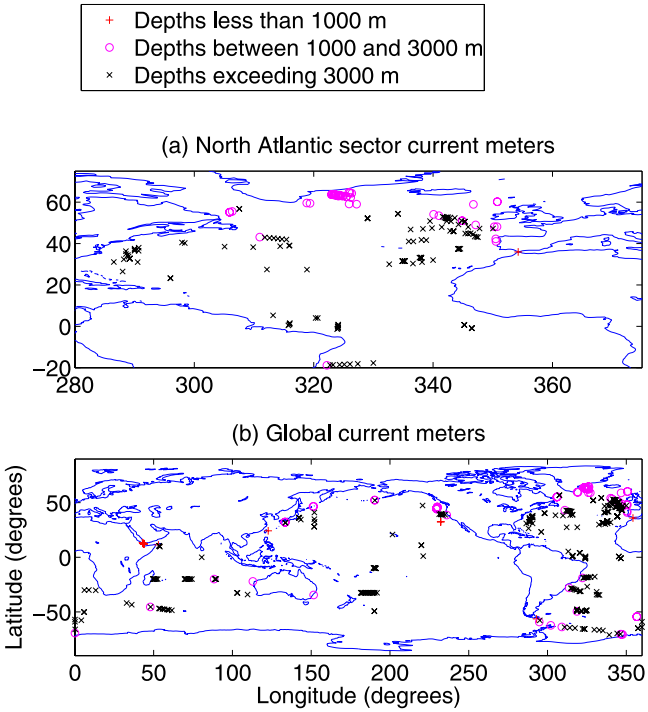

Figure 2. (a) Locations of 187 North Atlantic current meters deemed sufficiently near the seafloor (see text) and for which global DANLOM, NANLOM, and POP output, as well as output from the North Atlantic POP simulation, are available for comparison. (b) Locations of 382 moored current meters used in the global analysis of the global DANLOM, NANLOM, and POP simulations. Approximate seafloor depths of the moorings are also indicated in Figure 2.

database which satisfy all of our criteria is 382. A subset of these, numbering 187, can additionally be compared to the North Atlantic POP simulation. Figure 2a shows the locations of the 187 current meters used in the North Atlantic analysis, while Figure 2b shows the 382 current meters used in the global analysis.

4. Dissipation Formula

[20] The time-averaged dissipation rate at a model grid point (or mooring location) is computed as

$$\overline{D}(\theta,\phi) = \rho c_d \overline{|\mathbf{u}_b|^3} \tag{1}$$

[*Taylor*, 1919], where θ and ϕ are respectively the longitude and latitude of the grid point, ρ = 1035 kg m^{-3} is the average density of seawater, $|\mathbf{u}_b|$ is the magnitude of the bottom velocity vector, and overbars denote time averaging. In DANLOM and NANLOM we take the bottom velocity to be the velocity in the bottom (sixth) layer. In North Atlantic and global POP the bottom velocity is taken from the lowest active level of the 40 z-levels. This lowest level varies as a function of geographical location. Only "total" velocities are utilized in our study. A time mean is not removed from either model or mooring velocities. In ocean models, the quadratic drag coefficient c_d typically lies between 0.001 and 0.003. Observations indicate a somewhat wider range of plausible values [e.g., *Trowbridge and Lentz*, 1998; *Duncan et al.*, 2003]. The parameterization (1) does not cover the complex internal wave dynamics arising in topographically rough areas, which require an additional parameterization [e.g., *Jayne and St. Laurent*, 2001; *Garner*, 2005].

[21] The native values of c_d used in the model simulations are 0.003/0.002/0.001225/0.001225 for DANLOM/NANLOM/global POP/North Atlantic POP. We will present dissipation rates computed using the native c_d values, which would be the rates appropriate for an examination of model energy budgets. Another approach we follow is to regard the models as providing estimates of bottom velocity, which can be combined with any reasonable value of c_d to yield dissipation rates, irrespective of considerations of model energy budgets. We therefore also present dissipation rates computed using a common value of c_d = 0.0025 for all the simulations. The common value makes for easier comparison of results from the different simulations, as well as easier comparison with the observationally based dissipation estimates of *Sen et al.* [2008], in which c_d was also set to 0.0025.

5. Results

[22] The first goal of this section is to determine how realistic the bottom flows in the models are, through comparison to flows measured by near-bottom moored current meters. The second goal is to discuss the dissipation rates computed from the model bottom flows. Values of areally averaged dissipation will be given, and maps of the dissipation rates will be shown. The analysis will be done first in the North Atlantic, and then on a global scale.

[23] The model/data comparison will focus on values of $\overline{|\mathbf{u}_b|^3}$, since this quantity multiplied by $\rho\ c_d$ yields the dissipation rate. The model and mooring $\overline{|\mathbf{u}_b|^3}$ values will be plotted alongside each other as a function of seafloor depth. As noted earlier, there is reason to believe that NLOM will not perform as well in shallow waters as in abyssal waters. Additionally, scatterplots will be made of model versus mooring values of $\overline{|\mathbf{u}_b|^3}$. We display two different measures of the model values at the mooring sites: (1) the value of $\overline{|\mathbf{u}_b|^3}$ interpolated to the mooring location and (2) the model values, in 1° by 1° boxes centered on the mooring locations, which come closest to matching the mooring values. The two measures are denoted by "Interpolated" and "Best", respectively, in this paper. A third measure, the mean of model values over the 1° by 1° boxes, was also computed. The mean values are in most cases similar to the interpolated values. Hence for the sake of brevity we do not further discuss the mean values in this paper. The best measure is more forgiving than the interpolated measure, as it compares well with the data in cases where model $\overline{|\mathbf{u}_b|^3}$ fields contain values comparable to those in the moorings, but in slightly offset locations. In addition to displaying model/data comparisons at individual mooring sites, we will compare averages of the two model measures of $\overline{|\mathbf{u}_b|^3}$, taken over many mooring locations, to averages of the mooring values themselves. This exercise aids in gauging the skill of the models at predicting integrals of $\overline{|\mathbf{u}_b|^3}$ (hence dissipation) over large areas. In another test of model skill, we will compute the best values from model locations sampled randomly, to ascertain whether such sampling yields different results than sampling the models at the actual mooring locations.

5.1. North Atlantic Results

[24] We begin with plots of $\overline{|\mathbf{u}_b|^3}$ versus seafloor depth. Figure 3a shows the interpolated values of $\overline{|\mathbf{u}_b|^3}$ in the North Atlantic POP simulation, and in the North Atlantic sectors of the global DANLOM, NANLOM, and POP simulations, at the 187 North Atlantic mooring sites, as a function of the seafloor depth at the moorings. Mooring values of $\overline{|\mathbf{u}_b|^3}$ are also plotted. At the two current meter sites having seafloor depths less than 1000 m (both located at the Strait of Gibraltar), values of $\overline{|\mathbf{u}_b|^3}$ in North Atlantic POP are somewhat lower than those in the moorings. Interpolated $\overline{|\mathbf{u}_b|^3}$ values in the three global models are much too weak at these two locations. Note that in this paper we denote locations having seafloor depths less than 1000 m as "Shallow." In "Intermediate" depths (depths between 1000 and 3000 m), none of the three global models have interpolated $\overline{|\mathbf{u}_b|^3}$ values lying near the largest mooring values, while North Atlantic POP does have values lying close to this high level. On the other hand, for "Abyssal" waters (seafloor depths exceeding 3000 m), the interpolated $\overline{|\mathbf{u}_b|^3}$ values in all four models cluster at a level near that seen in the moorings.

[25] As is to be expected, there is a visually tighter fit between models and data in Figure 3b, which displays the best model values. Here North Atlantic and global POP perform well over all depths, with many of the $\overline{|\mathbf{u}_b|^3}$ values lying nearly on top of those seen in the moorings. The DANLOM and NANLOM best values continue to be much too small in shallow and intermediate depths, but lie at

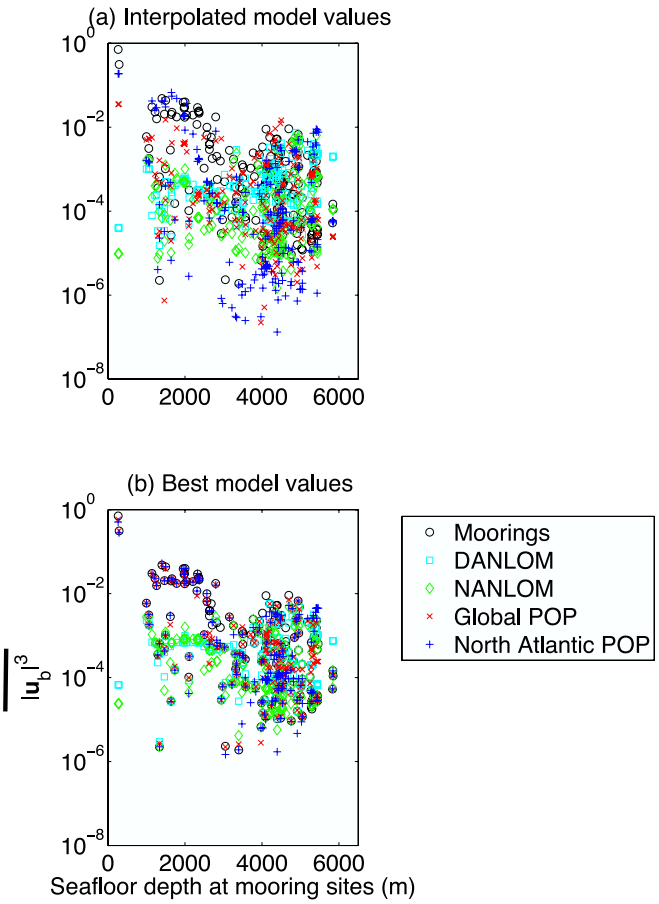

Figure 3. Values of $\overline{|\mathbf{u}_b|^3}$ computed from 187 moored near-bottom North Atlantic current meters, alongside values at the mooring locations from North Atlantic POP and the North Atlantic sectors of DANLOM, NANLOM, and global POP, plotted versus the seafloor depths of the moorings. (a) Model values interpolated to the mooring coordinates. (b) Model values, taken from 1° by 1° boxes centered on the moorings, which compare most closely to the mooring values. Units of $\overline{|\mathbf{u}_b|^3}$ are $m^3\ s^{-3}$.

approximately the same level as the mooring values for seafloor depths exceeding 3000 m.

[26] Next we display scatterplots of model versus mooring values of $\overline{|\mathbf{u}_b|^3}$. In Figures 4a and 4b we respectively show the interpolated and best model $\overline{|\mathbf{u}_b|^3}$ values at the mooring sites, plotted against the mooring $\overline{|\mathbf{u}_b|^3}$ values. Extra lines are drawn at a 45° angle (all points would lie along these lines if the models matched the data perfectly). In Figure 4a, the scatter is considerable, even with North Atlantic POP. The best values give a tighter fit, especially in the case of the two POP simulations. In all four simulations, and for both interpolated and best measures, model values display a weak bias with respect to the mooring values, as seen in the greater number of points below the 45° line than above.

[27] The indications thus far are that the models have some difficulty matching individual current meter records. However, we have also seen visual indications that the model $\overline{|\mathbf{u}_b|^3}$ values cluster at approximately the same level as the mooring values, at least in certain depth ranges. We quantify this by comparing averages of model and current meter $\overline{|\mathbf{u}_b|^3}$ values over many mooring sites. We define

$$\gamma = \frac{\sum_{i=1}^{M} \overline{|\mathbf{u}_{bmodel}|^3_{,i}}}{\sum_{i=1}^{M} \overline{|\mathbf{u}_{bmooring,i}|^3}}, \tag{2}$$

where i is an index of the mooring locations, M is the total number of moorings over which γ is computed, $\overline{|\mathbf{u}_{bmodel}|^3_{,i}}$ is the measure of the model $\overline{|\mathbf{u}_b|^3}$ values at mooring location i, and $\overline{|\mathbf{u}_{bmooring,i}|^3}$ is the mooring value of $\overline{|\mathbf{u}_b|^3}$ at location i. Table 1 gives values of γ in the North Atlantic for the four models discussed, for the two measures of model $\overline{|\mathbf{u}_b|^3}$

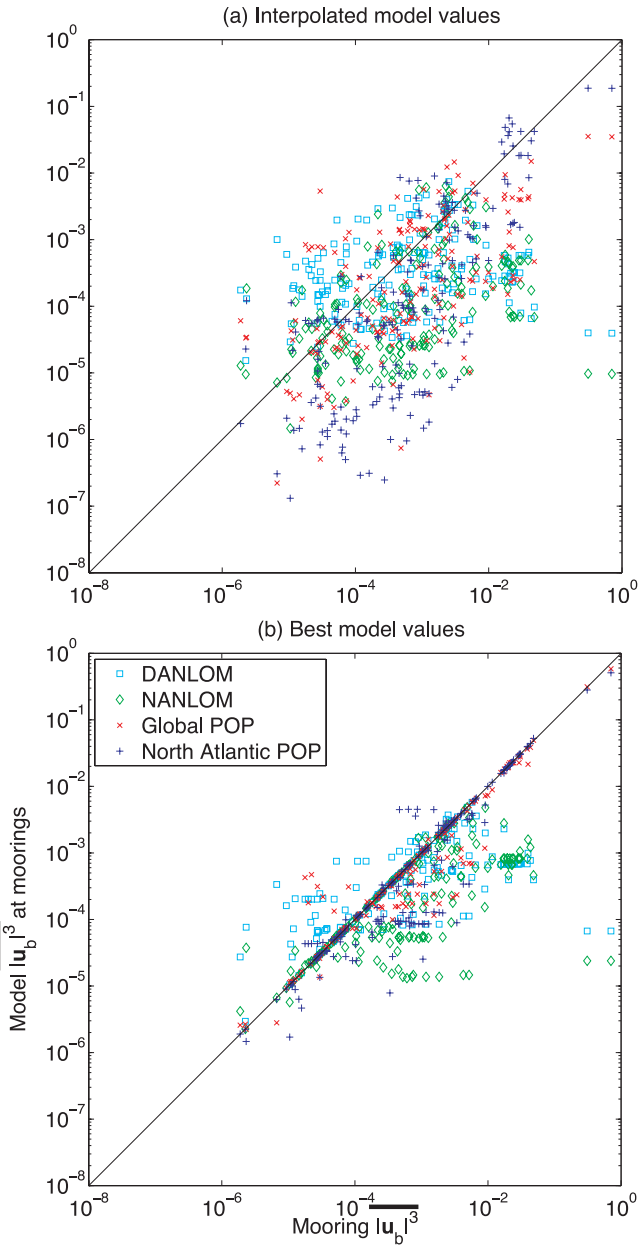

Figure 4. As in Figure 3 except that model $\overline{|\mathbf{u}_b|^3}$ values are plotted versus mooring $\overline{|\mathbf{u}_b|^3}$ values.

Table 1. Values of γ Computed Over 187 Moored Near-Bottom Current Meters in the North Atlantic[a]

Model	Measure	γ		
		Shallow	Intermediate	Abyssal
DANLOM	Interpolated	0.000078	0.025	0.89
DANLOM	Best	0.00013	0.051	0.72
NANLOM	Interpolated	0.000019	0.026	0.50
NANLOM	Best	0.000047	0.055	0.48
Global POP	Interpolated	0.069	0.16	0.85
Global POP	Best	0.88	0.90	0.77
North Atlantic POP	Interpolated	0.37	0.86	0.73
North Atlantic POP	Best	0.78	1.0	0.78
North Atlantic POP	Best random	0.057	0.15	0.32

[a]The meanings of interpolated, best, and best random as measures of the model are explained in the text. Shallow denotes locations with mooring seafloor depths less than 1000 m (M = 2), intermediate denotes depths between 1000 and 3000 m (M = 48), and abyssal denotes depths exceeding 3000 m (M = 137). See equation (2) and surrounding text for definition of γ. M denotes number of current meters.

values, and for three ranges (shallow, intermediate, abyssal) of seafloor depths at the mooring sites. In shallow and intermediate waters, consistent with the discussion of Figure 3, the γ values for DANLOM and NANLOM are much less than unity, for North Atlantic POP are of order unity (lying between 0.37 and 1.0) for both measures, and for global POP are of order unity for the best measure only. In abyssal waters, the γ values for all models and both model measures are of order one, lying between 0.48 and 0.89.

[28] Table 1 contains a somewhat counterintuitive result (some of the best γ values are lower than the corresponding interpolated γ values). We use a simple example to illustrate how an interpolated $\overline{|\mathbf{u}_b|^3}$ value could actually match the $\overline{|\mathbf{u}_b|^3}$ value at a single mooring more closely than does the best $\overline{|\mathbf{u}_b|^3}$ value. Suppose that the mooring value is "4" (arbitrary units, for simplicity) and that the four surrounding model grid points, all lying equal distances from the mooring, have $\overline{|\mathbf{u}_b|^3}$ values of 1, 3, 6, and 6. The model interpolated $\overline{|\mathbf{u}_b|^3}$ value would then be 4, exactly matching the mooring value, while the model best $\overline{|\mathbf{u}_b|^3}$ value of 3 does not. Because it is possible at a single mooring for the interpolated $\overline{|\mathbf{u}_b|^3}$ value to perform better than the best $\overline{|\mathbf{u}_b|^3}$ value, it is also possible for interpolated values to perform better when averages are taken over many mooring sites.

[29] It is fair to ask whether order one values of γ really do demonstrate model skill in matching averages of $\overline{|\mathbf{u}_b|^3}$ over large areas. This is particularly true given that the best values are constructed to compare well to the mooring values. On the other hand, the best values will only compare well to observations if small subdomains of the model contain at least one grid point having flows of approximately correct magnitude. With this in mind, we performed the following exercise as a further test of model skill. For each current meter in a particular depth range, we picked a grid point lying in the same depth range (as defined by the bottom topography used in the model), at random, from the North Atlantic POP simulation. We then found the model $\overline{|\mathbf{u}_b|^3}$ values, taken from 1° by 1° boxes centered on these random model grid points, which compare most closely to the mooring values of $\overline{|\mathbf{u}_b|^3}$. The exercise was repeated several times, and an average was taken over all the exercises, to settle on a value of γ denoted "Best Random" in the last line of Table 1. The best random γ values for North Atlantic POP are substantially smaller than the best and interpolated values, for all three depth ranges. The best random values were also calculated in the abyss for the three global models. The topography used to define seafloor depths in DANLOM and NANLOM for this exercise is the source topography, i.e., the topography before the vertical compression used in NLOM takes place. The abyssal best random values are 0.77 for DANLOM, 0.25 for NANLOM, and 0.29 for global POP. Except in the case of DANLOM, these values are substantially smaller than the best and interpolated γ values, suggesting some degree of model skill in predicting abyssal flows. We will return to this point in section 5.2.

[30] Since many of the γ values in Table 1 are of order unity, at least in specific depth ranges, we infer that all of the models may yield reasonable order-of-magnitude estimates of areally integrated dissipation. Table 2 lists the dissipations $[\overline{D}]$ integrated over the North Atlantic, computed as

$$[\overline{D}] = \int \overline{D}(\theta,\phi)\, dA = \int \rho c_d \overline{|\mathbf{u}_b|^3}\, dA, \tag{3}$$

where the [ ] operator represents an areal integration over the domain defined by the North Atlantic POP simulation, and dA is an element of area. Values are given for shallow, intermediate, and abyssal depths. Again, the source topography is used to define depths in DANLOM and NANLOM for these computations. Total denotes an integration over all depths. For each simulation, dissipation rates are given for two values of c_d: the native value used in the simulation, and a common value of 0.0025. We note that the native dissipations are within a factor of 2 or less of the common dissipations, and concentrate our discussion on the latter, since intercomparison between different simulations is easier in this case. The dissipations in DANLOM and NANLOM take place primarily in the abyss. Conversely, in

Table 2. Values of Dissipation Rate $[\overline{D}]$ in the North Atlantic[a]

Model	c_d	$[\overline{D}]$			
		Shallow	Intermediate	Abyssal	Total
DANLOM	Native	0.00059	0.0079	0.13	0.14
NANLOM	Native	0.00042	0.0029	0.023	0.026
Global POP	Native	0.028	0.010	0.0095	0.048
North Atlantic POP	Native	0.034	0.011	0.016	0.061
DANLOM	Common	0.00049	0.0066	0.11	0.11
NANLOM	Common	0.00053	0.0036	0.029	0.033
Global POP	Common	0.058	0.021	0.019	0.099
North Atlantic POP	Common	0.069	0.022	0.033	0.12

[a]Total denotes an integration over all depths. Computations are done with both native values of c_d (0.003 for DANLOM, 0.002 for NANLOM, 0.001225 for global POP, and 0.001225 for North Atlantic POP) and a common value of c_d = 0.0025. In TW.

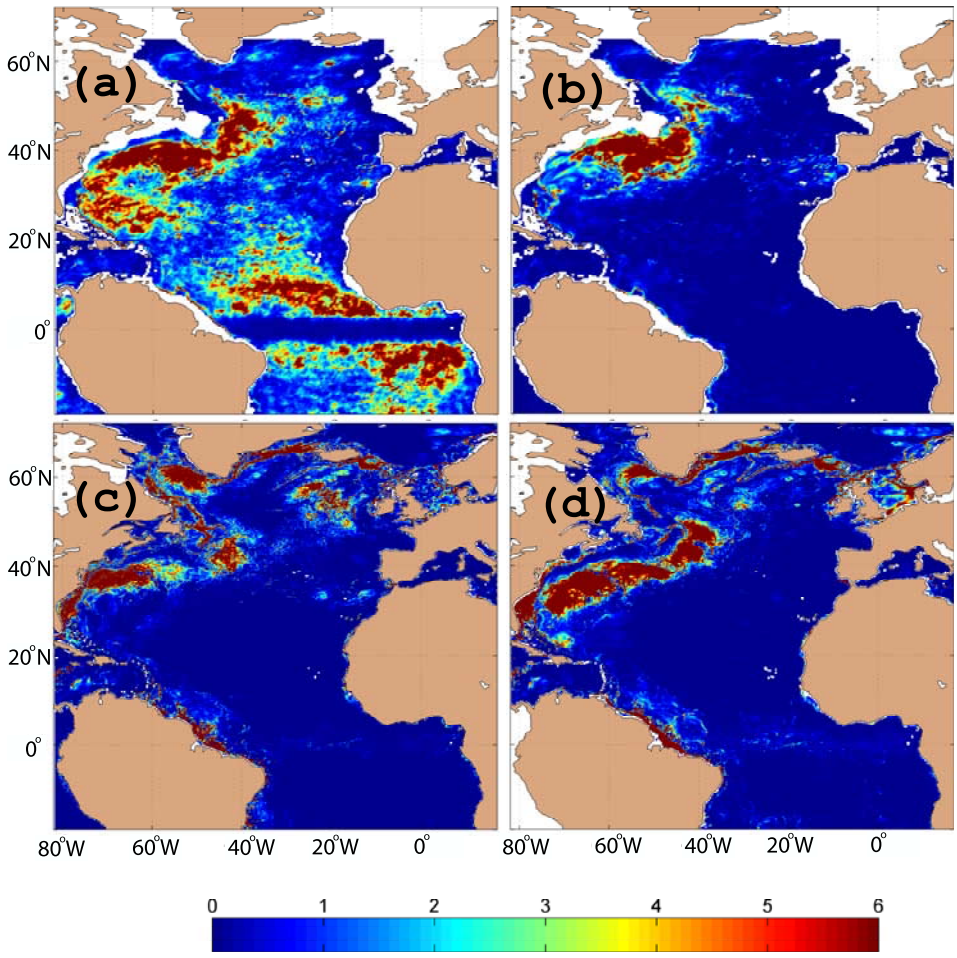

Figure 5. Maps of dissipation rate (mW m^{-2}) in the North Atlantic sectors of the three global models (a) DANLOM, (b) NANLOM, and (c) global POP, and (d) in North Atlantic POP. Figures 5a, 5b, 5c, and 5d extend to 72°N. A common value of $c_d = 0.0025$ was used to make Figures 5a, 5b, 5c, and 5d.

both North Atlantic and global POP, a substantial fraction (about 70–80%) of the total dissipation takes place in shallow and intermediate depths. While it is not difficult to find inconsistencies between the simulations, there is also some room for optimism. The $[\overline{D}]$ values for global POP are within a factor of 1.8 or less of those in North Atlantic POP, over all three depth ranges. The NANLOM abyssal $[\overline{D}]$ value is very close to that in North Atlantic POP and is within a factor of 1.5 of that in global POP. The total $[\overline{D}]$ values for the four models lie within a factor of about 4 of each other. To us the discussion of Tables 1 and 2 suggests that the abyssal and total dissipations in all four simulations, and the shallow and intermediate dissipations in the two POP simulations, are accurate to factors of about 4 or better.

[31] We now examine maps of the dissipation rates. For ease of comparison, Figure 5 displays the results of all four simulations mapped onto the same grid, which has a northern boundary at 72°N. Also for ease of comparison, Figures 5a, 5b, 5c, and 5d are made using the common c_d value of 0.0025. The maps feature important similarities, for instance a strong Gulf Stream system, as well as clear differences. Both POP simulations feature large dissipation rates along the northeast coast of South America, in waters between Great Britain and Iceland, along the east coast of Greenland, and in the Labrador Sea, that are not present in DANLOM and NANLOM. In the Gulf Stream region, large dissipations take place over a greater areal extent in DANLOM and North Atlantic POP than in NANLOM and global POP. In DANLOM there are patches of large dissipation just off of the equator (starting at about ±5°) which are not seen in the other models. Some of the tropical Atlantic current meters in our database exhibit $\overline{|\mathbf{u}_b|^3}$ values comparable to those seen at ±5° off of the equator in DANLOM, but these current meters lie within 1–2° of the equator. Thus it is difficult to determine with the data at hand whether these patches are real or artificial. The patches may result from the scheme used in DANLOM to propagate assimilated information at the surface to deep layers of the model [*Hurlburt et al.*, 1990]. The statistical inference is performed globally, but the geostrophic correction to velocities is tapered off between 5 and 2 degrees. The lack of a geostrophic adjustment to the currents along the equator after assimilation of sea surface height evidently results in low values of along-equatorial dissipation in DANLOM that resemble those in the other models. The patches of large dissipation in near-equatorial DANLOM are in part responsible for the larger $[\overline{D}]$ and best random γ values seen in abyssal DANLOM than in the abyssal regions of the other models.

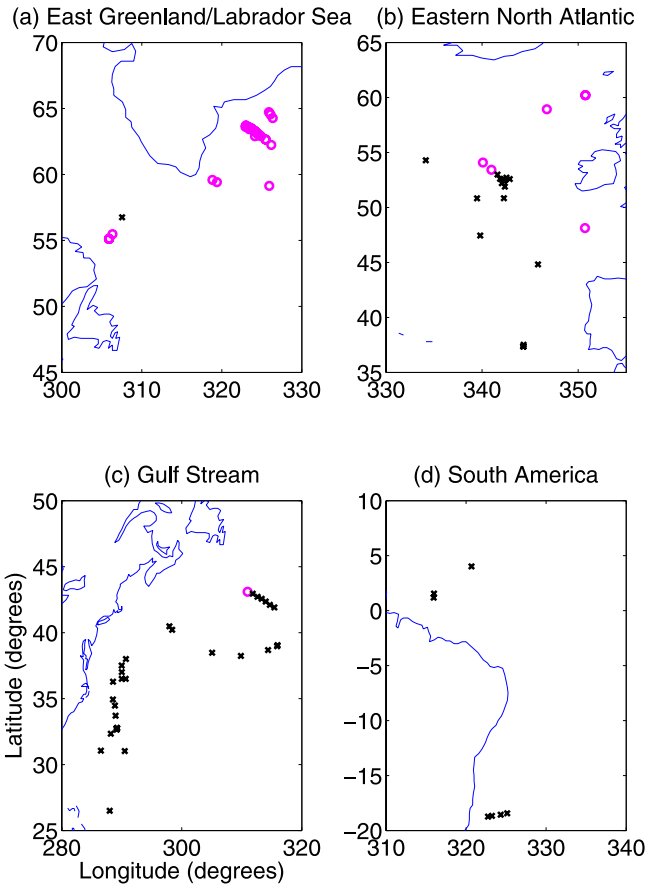

Figure 6. Current meters with large time-averaged currents (see text) in four subregions of the North Atlantic domain. Values of M (number of moorings) and $\overline{D}_{average} = 0.0025\ \rho\ \overline{|\mathbf{u}_b|^3}$ averaged over all of the moorings (units in mW m^{-2}), are listed below. (a) East Greenland/Labrador Sea ($M = 35$, $\overline{D}_{average} = 40$). (b) Eastern North Atlantic ($M = 27$, $\overline{D}_{average} = 8.9$). (c) Gulf Stream ($M = 31$, $\overline{D}_{average} = 6.7$). (d) South America ($M = 7$, $\overline{D}_{average} = 6.7$). As in Figure 2, black crosses denote locations with seafloor depths exceeding 3000 m, and magenta circles denote locations with seafloor depths between 1000 and 3000 m.

[32] The differences in the four maps shown in Figure 5 motivate us to examine how well strong currents in specific subregions are captured in the models. Figure 6 shows four such subregions of the North Atlantic domain. In this analysis we use only current meters for which $0.0025\ \rho\ \overline{|\mathbf{u}_b|^3}$ exceeds 1 mW m^{-2}. Such current meters account for the bulk of the $\overline{|\mathbf{u}_b|^3}$ averaged across all of the current meters in these subregions. We exclude the two current meters in the Strait of Gibraltar, which would otherwise dominate the statistics of the Eastern North Atlantic (Figure 6b), and which have already been extensively compared to the models, in the "Shallow" column of Table 1. Table 3 displays the γ values computed in the four subregions. For the sake of brevity, only best γ values are shown (interpolated γ values are generally lower, at times much lower). All four simulations capture the Gulf Stream well, with γ values ranging from 0.68 to 1.1. All four simulations perform reasonably well in the region we denote by "South America", with γ values ranging from 0.30 to 0.39. The strong currents along the East Greenland coast and Labrador Sea (mainly in waters of intermediate depth) are captured well by the two POP simulations, but not by the two NLOM simulations, as expected given the differences seen in Figure 5. Similarly, the strong currents in the Eastern North Atlantic (also mainly in waters of intermediate depth) are much better captured by POP than by NLOM. The agreement between the POP simulations and current meter records in these intermediate-depth locations in the North Atlantic gives us confidence that the strong currents along continental edges may be reasonably accurate in POP. This will be important in section 5.2, where we will see that global POP has strong currents along continental edges throughout the globe, usually in locations where no current meter data is available for model validation.

5.2. Global Results

[33] As in the North Atlantic analysis, we begin with plots of model $\overline{|\mathbf{u}_b|^3}$ values versus seafloor depth and versus mooring $\overline{|\mathbf{u}_b|^3}$ values. Figure 7 shows the interpolated and best values of $\overline{|\mathbf{u}_b|^3}$ in the three global simulations, at the 382 global mooring sites, together with the mooring $\overline{|\mathbf{u}_b|^3}$ values, as a function of the seafloor depth at the moorings. Figure 7b, displaying best values, is visually tighter than Figure 7a, displaying interpolated values. In shallow and intermediate depths, the interpolated $\overline{|\mathbf{u}_b|^3}$ values in all three global simulations are systematically smaller than the current meter $\overline{|\mathbf{u}_b|^3}$ values. This is especially true for the two NLOM simulations. The best values of global POP compare more closely to observations in shallow and intermediate depth waters than do either the interpolated POP values, or the best values from DANLOM and NANLOM. In abyssal waters, for both interpolated and best measures, all three global simulations have $\overline{|\mathbf{u}_b|^3}$ values that appear to lie at the same approximate level as the mooring values. In Figure 8, we show scatterplots of the two measures of model $\overline{|\mathbf{u}_b|^3}$ values at the mooring sites plotted against the mooring values. As in Figure 4, the scatter is considerable, the number of low outliers exceeds the number of high outliers, and tighter fits occur when the best model values are used, especially in the case of global POP.

[34] Once again, we compute values of γ, using both interpolated and best values, but this time across the 382 global mooring sites, and using only the three global simulations (Table 4). In shallow and intermediate depths, γ is small for all three global models, except when global POP is measured by its best values. In abyssal waters, γ

Table 3. Values of γ Computed in Subregions of the North Atlantic[a]

Region	DANLOM	NANLOM	Global POP	North Atlantic POP
East Greenland/Labrador Sea	0.051	0.057	0.89	0.99
Eastern North Atlantic	0.19	0.058	0.99	0.91
Gulf Stream	0.84	0.68	0.92	1.1
South America	0.31	0.31	0.30	0.39

[a]Values were computed from best $\overline{|\mathbf{u}_b|^3}$ values of the simulations in the four subregions of the North Atlantic domain shown in Figure 6.

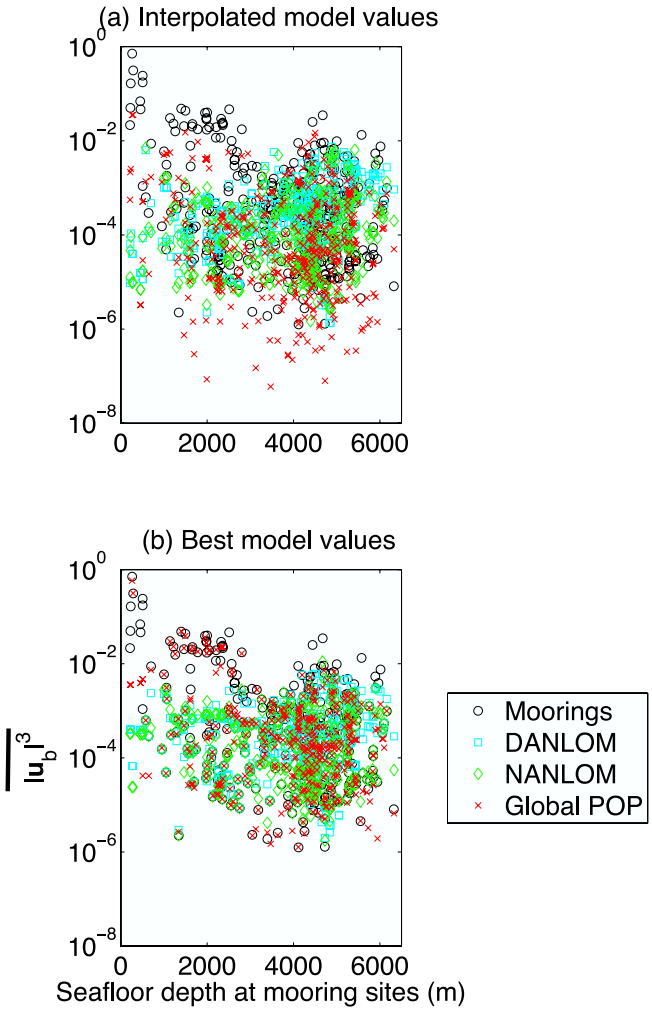

Figure 7. As in Figure 3 except that the comparison is global. Only the three global simulations are shown. All 382 near-bottom current meters in the global database are used.

takes on order one values (from 0.37 to 0.73) for all three simulations and for both measures of model $\overline{|\mathbf{u}_b|^3}$ values. The best random values of global POP (see the last line in Table 4) are considerably lower than the best values, for all three depth ranges. The abyssal best random values for DANLOM and NANLOM are 0.46 and 0.25, respectively, lower than the interpolated and best values in the abyss for these models. The DANLOM North Atlantic abyssal best random γ value is the only one of several best random values we have calculated that is not smaller than the corresponding best and interpolated γ values. All of this suggests to us that the simulations used in this paper do have some skill in putting large $\overline{|\mathbf{u}_b|^3}$ values in approximately correct locations. To add to this point, we reiterate the results of *Hurlburt and Hogan* [2000] and *Hogan and Hurlburt* [2000], that abyssal eddy kinetic energies are a strong function of horizontal resolution. A glance at Figure 12 of *Hurlburt and Hogan* [2000] makes clear that if γ values were to be calculated from NLOM simulations run with horizontal resolutions of 1/8° or less, they would be much lower than the γ values calculated here. This also suggests that the simulations we have chosen to analyze in this paper have some degree of skill, more so than other simulations we could have chosen.

[35] The globally integrated dissipations $[\overline{D}]$ for the three global simulations are shown in Table 5. As in the North Atlantic, most of the dissipation in DANLOM and NANLOM takes place in abyssal waters, while about 70% of the dissipation in global POP takes place in shallow and intermediate waters. Depending on whether native or common values of c_d are used, the $[\overline{D}]$ values integrated over all depths range from 0.14–0.65 TW in the three simulations.

[36] Globally integrated dissipations broken down by latitude instead of by seafloor depth are displayed in Table 6. In NANLOM, the dissipation in tropical latitudes

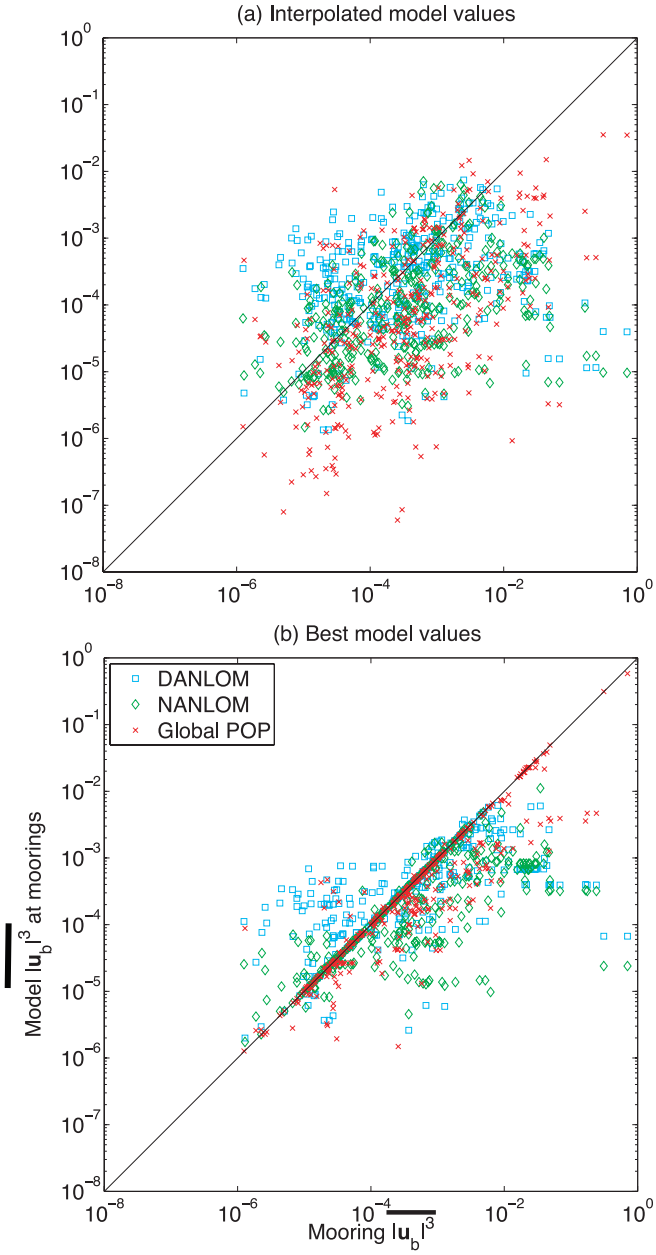

Figure 8. As in Figure 4 except that the comparison is global. Only the three global simulations are shown. All 382 near-bottom current meters in the global database are used.

Table 4. As in Table 1, but Computed Across All 382 Near-Bottom Current Meters in the Global Database[a]

		γ		
Model	Measure	Shallow	Intermediate	Abyssal
DANLOM	Interpolated	0.0041	0.031	0.73
DANLOM	Best	0.0037	0.060	0.62
NANLOM	Interpolated	0.0043	0.028	0.37
NANLOM	Best	0.0023	0.060	0.40
Global POP	Interpolated	0.045	0.15	0.40
Global POP	Best	0.52	0.83	0.46
Global POP	Best random	0.048	0.10	0.15

[a]The number of moorings M equals 14, 94, and 274 for shallow, intermediate, and abyssal depths, respectively.

is about 14% of the total. In global POP and DANLOM, the tropical dissipation represents about 30% and 40%, respectively, of the total. The large tropical dissipations occur in different locations in global POP than in DANLOM. As discussed previously, DANLOM, unlike the other simulations, has large patches of high dissipation in abyssal near-equatorial regions. In global POP, the tropical dissipations are largest in regions of strong currents along continental edges (see Figure 9, to be described shortly). In DANLOM and global POP, about 20% of the dissipation occurs in the Southern Ocean, while in NANLOM, about 40% of the dissipation occurs there. Similarly substantial ratios of Southern Ocean to total dissipation were seen in the observationally based estimates of *Sen et al.* [2008]. However, as in the paper by *Sen et al.* [2008], none of the Southern Ocean $[\overline{D}]$ values is as large as the wind-power input into the Southern Ocean, which represents about 70% of the global integral [*Wunsch*, 1998].

[37] Global maps of the dissipation rates computed from the three global simulations, and from the $[\overline{D}_3]$ observationally based estimate of *Sen et al.* [2008] (adapted here from their Figure 3a), are shown in Figure 9. A drag coefficient value of $c_d = 0.0025$ is used to construct all four maps. Note that $[\overline{D}_3] = 0.21$ TW. Some of the well-known abyssal currents, such as the Gulf Stream, Kuroshio, Agulhas, and Antarctic Circumpolar Current, are clearly visible in all four maps. The deep currents are generally more pronounced (in both areal extent and intensity) in the DANLOM map than in the other three maps. On the other hand, Figure 9c shows several places where global POP has strong currents in shallow waters, which are not present in DANLOM or NANLOM. These are not present in the observationally based estimate either, since this only covers locations with seafloor depths of 3000 m or greater. The DANLOM map shows many patches of high dissipation in basin interiors (see, for instance, the patch located to the northeast of New Zealand) and just off the equator (especially in the Atlantic) which are not seen in the other maps. These features are in part responsible for the larger global dissipation rate and best random γ values computed from DANLOM. The visual agreement between model-based and observationally based estimates (or amongst different model estimates) does not appear to be as close for abyssal flows as it is for surface flows (compare Figure 9 here to Figure 12 from *Maltrud and McClean* [2005]). Nevertheless there are enough similarities between the maps shown in Figure 9 to give us some degree of confidence in the result that the globally integrated dissipation rates are substantial.

[38] The area of low dissipation in the southeast Pacific of DANLOM results from an intentional suppression of the abyssal velocities in order to prevent an unrealistic Antarctic Circumpolar Current pathway in this area (see Figure 9b). This suppression was done in the model run, not in the analysis, and thus cannot be undone. We estimate the impact of this patch of suppressed velocities on the DANLOM $[\overline{D}]$ values in two ways: by computing the ratio of the area of the patch to the area of the remaining grid points in the model, and by computing the $[\overline{D}]$ value in NANLOM with velocities in this patch set to zero. Both methods suggest that the patch reduces the DANLOM $[\overline{D}]$ value by about 3%.

[39] As in section 5.1, we conclude with an analysis of a few subregions having strong currents. Figure 10 shows the locations of current meters for which $0.0025\ \rho\ \overline{|\mathbf{u}_b|^3}$ exceeds 1 mW m^{-2} in regions we denote by "Kuroshio", "Southern South Atlantic", and "Southern Africa". Table 7 shows the best γ values in these regions computed from the three global simulations. The γ values range from 0.12 to 0.74, with DANLOM γ values being near order one most consistently. For global POP, interpolated γ values (not shown) are considerably lower (by factors of 5–7) than the best γ values. Consistent with appearances in Figure 9, the γ values suggest that some prominent abyssal currents are too weak in NANLOM and in global POP.

6. Frequency Content of Model Flows and Effects of Infrequent Temporal Sampling

[40] The calculations presented thus far are based on model velocities that are not low-pass filtered. The large size of the model outputs makes computing low-pass filtered velocities at all of the model grid points impractical. However, we did test the frequency content of the velocities at a small number of locations, by writing out NANLOM velocities at the abyssal mooring sites, and applying a 15-day low-pass filter before computing the $\overline{|\mathbf{u}_b|^3}$ values. (We cannot apply a 3-day low-pass filter, as we did with the current meter data, since the model output is every 3 days). The average of $\overline{|\mathbf{u}_b|^3}$ taken over all the deep water mooring sites is reduced by only 6% from the values presented earlier, demonstrating that the abyssal NANLOM bottom layer flows, at least, are predominantly low frequency. In contrast, if we subsample current meter data every 3 days (the NANLOM sampling period) and then apply a 15-day filter, the average of $\overline{|\mathbf{u}_b|^3}$ computed over all of the mooring sites is reduced by much larger amounts, up to 40%, depending on the depth ranges considered. Alternatively, if we use the mooring data as is (sampled very frequently)

Table 5. As in Table 2, but Computed Globally for the Three Global Simulations

		$[\overline{D}]$			
Model	c_d	Shallow	Intermediate	Abyssal	Total
DANLOM	Native	0.0025	0.041	0.60	0.65
NANLOM	Native	0.0017	0.017	0.14	0.16
Global POP	Native	0.085	0.018	0.042	0.14
DANLOM	Common	0.0021	0.034	0.50	0.54
NANLOM	Common	0.0022	0.021	0.18	0.20
Global POP	Common	0.17	0.036	0.085	0.29

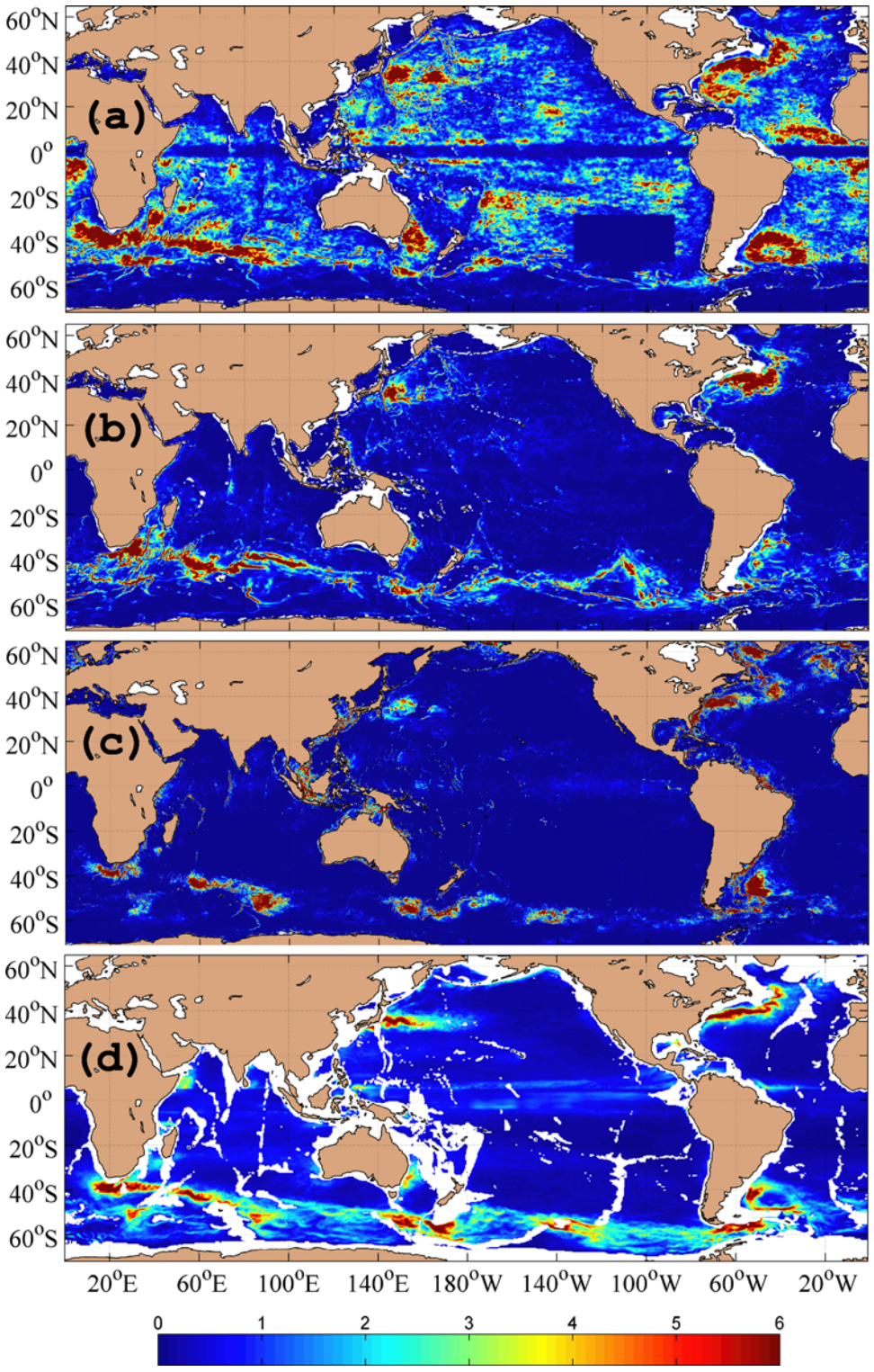

Figure 9. Maps of dissipation rate (mW m^{-2}) in the three global models (a) DANLOM, (b) NANLOM, and (c) global POP, and (d) in the $[\overline{D}_3]$ observationally based estimate of *Sen et al.* [2008]. Figures 9a, 9b, 9c, and 9d extend to 65°N. A common value of $c_d = 0.0025$ was used to make Figures 9a, 9b, 9c, and 9d. Note that the *Sen et al.* [2008] estimate shown here only covers seafloor depths exceeding 3000 m.

Table 6. As in Table 5, but Divisions Are by Latitude Instead of by Seafloor Depth[a]

Model	c_d	$[\overline{D}]$ Tropical	Extratropical	Southern Ocean	Total
DANLOM	Native	0.27	0.38	0.13	0.65
NANLOM	Native	0.022	0.14	0.064	0.16
Global POP	Native	0.043	0.10	0.030	0.14
DANLOM	Common	0.22	0.32	0.11	0.54
NANLOM	Common	0.028	0.17	0.080	0.20
Global POP	Common	0.087	0.21	0.062	0.29

[a]Tropical denotes latitudes equatorward of 23.5°, extratropical denotes latitudes poleward of 23.5°, and Southern Ocean denotes latitudes south of 40°S. Total denotes integration over all latitudes.

and low-pass it with just a 3-day filter, the average of $\overline{|\mathbf{u}_b|^3}$ calculated over all of the mooring sites is reduced by 20% or more [*Sen et al.*, 2008]. Both exercises demonstrate that high-frequency motions are much more prominent in current meter data than in the simulations used in this paper.

[41] The interannual variability of globally integrated dissipation appears to be small. We analyzed year 2002 of global POP, and found little difference in the dissipation rates from those presented in section 5 using year 2003. Analysis of a separate year of DANLOM output from that used here indicates that it also shows little interannual variability in the dissipation rate.

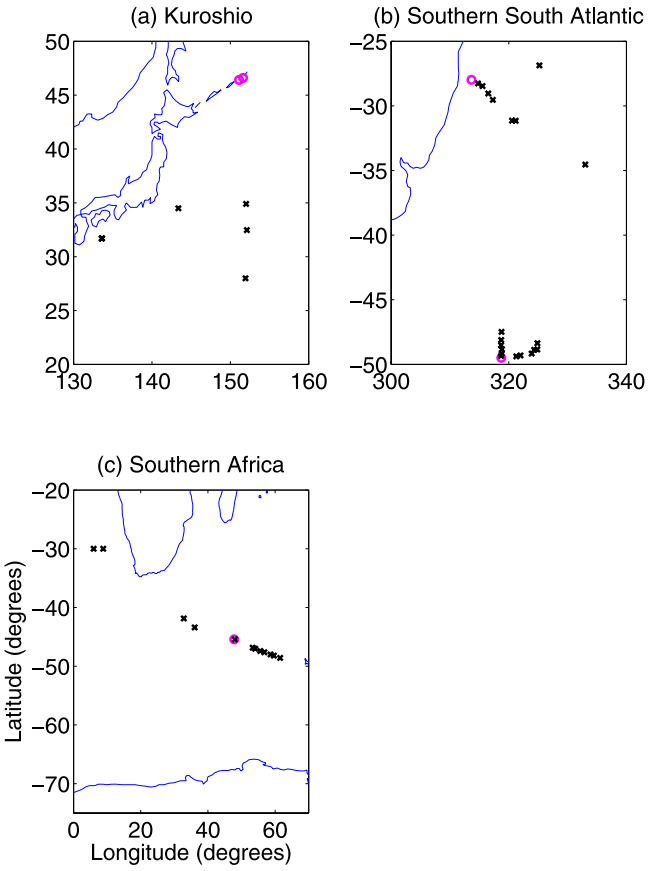

Figure 10. As in Figure 6, but for three subregions outside of the North Atlantic domain. (a) Kuroshio ($M = 8$, $\overline{D}_{average} = 12$). (b) Southern South Atlantic ($M = 22$, $\overline{D}_{average} = 22$). (c) Southern Africa ($M = 13$, $\overline{D}_{average} = 3.5$).

Table 7. As in Table 3, but for the Three Subregions Outside of the North Atlantic Shown in Figure 10

Region	DANLOM	NANLOM	Global POP
Kuroshio	0.40	0.19	0.32
Southern South Atlantic	0.31	0.16	0.12
Southern Africa	0.71	0.74	0.36

[42] High-frequency motions will be aliased into the model output, because of the infrequent temporal sampling of model snapshots. However, *McClean et al.* [2002] showed that the error introduced by infrequent sampling was minimal, for the case of surface kinetic energy in daily snapshots of North Atlantic POP. Here we examine the impact of subsampling on one year of output from another simulation of nonassimilative NLOM, which we denote by NANLOM2. The NANLOM2 run is similar to the NANLOM run, except that it contains the same patch of suppressed abyssal velocities in the South Pacific seen in DANLOM (which is why we didn't use it in section 5), has a slightly different c_d value (0.003), and most importantly, saved snapshots of model output more frequently, every 6 hours. For the sake of comparison, we also examine the impact of subsampling on the unfiltered current meter data, which as we have discussed contains stronger high-frequency flows than the models.

[43] Figure 11 shows the main results of our investigations, histograms of the quantity

$$\alpha = \frac{\overline{|\mathbf{u}_b|^3_{I2}} - \overline{|\mathbf{u}_b|^3_{I1}}}{\overline{|\mathbf{u}_b|^3_{I1}}}, \tag{4}$$

where $I2$ represents a coarser sampling interval, and $I1$ a finer interval, of the same data set. Figure 11a shows histograms of α for the data set of near-bottom current meters, where $I2 = 6$ hours and $I1$ represents the "source" sampling. The source sampling is the sampling given in the mooring database, which ranges from 15 min to 3 hours depending on the particular mooring. To avoid small numbers in the denominator of α, we also use only those moorings for which $0.0025\ \rho\ \overline{|\mathbf{u}_b|^3_{I1}}$ exceeds 1 mW m^{-2}. There are 224 such moorings. Six of the moorings are sampled at 3-hour intervals, while the remainder are sampled at intervals of 2 hours or finer, most commonly 1 hour. Figure 11a shows that for most of the current meters, subsampling at 6-hour intervals yields nearly the same value of $\overline{|\mathbf{u}_b|^3}$ as obtained from the more frequent source sampling. This suggests that the 6-hour sampling interval in NANLOM2 is sufficiently fine for it to serve as an adequate "control" (assumed to have relatively little aliasing) for an analysis on the impacts of infrequent sampling. The histogram of α values computed from daily subsamples ($I2 = 1$ day) and $I1$ still representing the source sampling is noticably wider (Figure 11b). Therefore a substantial number of moorings are adversely affected by 1-day subsampling. Because the difference between 6 hourly subsampling and source sampling is small (Figure 11a), and because NANLOM2 uses 6 hourly sampling, we use the 6 hourly sampling as a baseline ($I1 = 6$ hours) in the mooring data to test the effects of the infrequent temporal sampling of

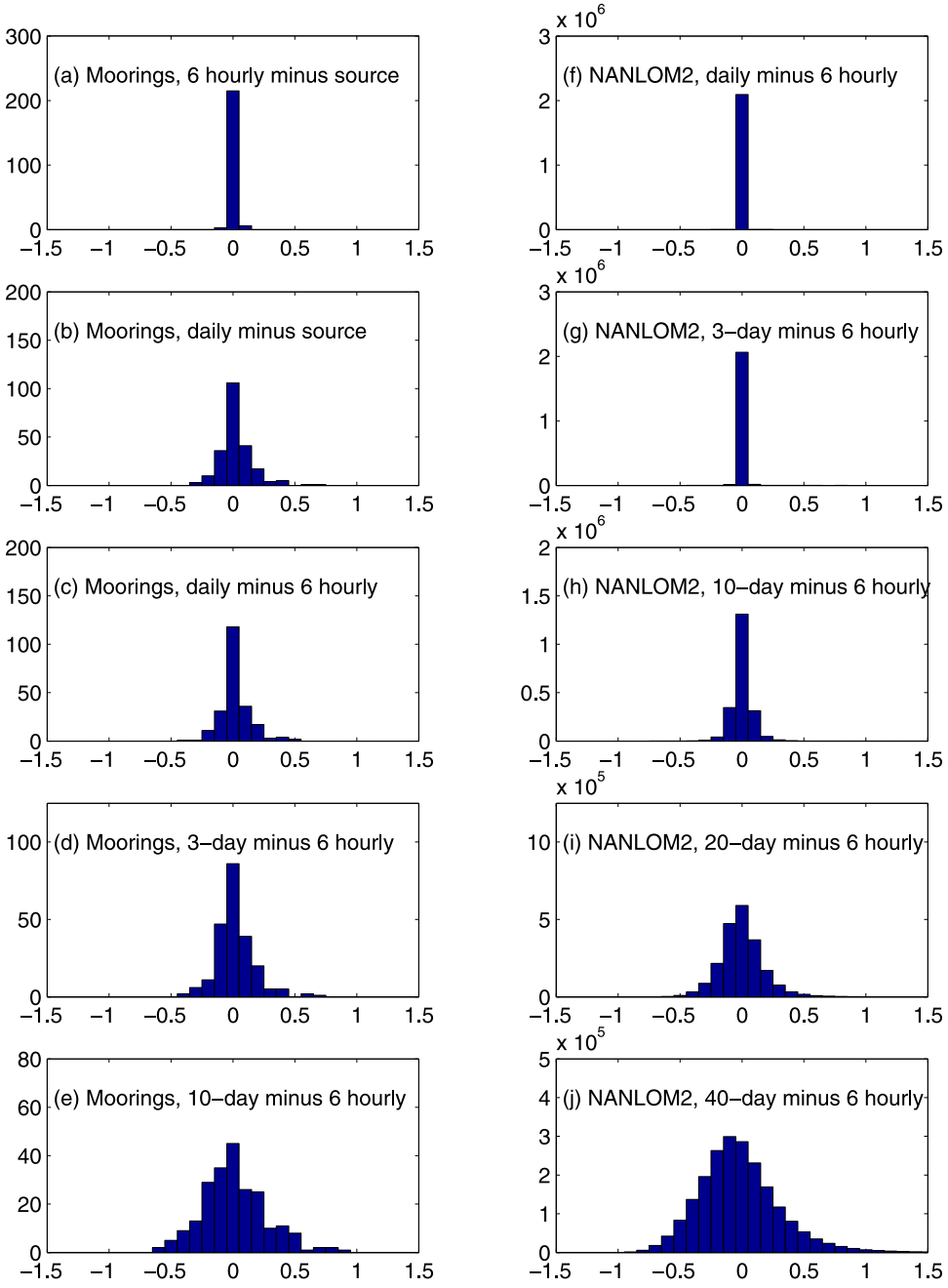

Figure 11. Histograms of $\alpha = \frac{\overline{|\mathbf{u}_b|^3_{I2}} - \overline{|\mathbf{u}_b|^3_{I1}}}{\overline{|\mathbf{u}_b|^3_{I1}}}$, where $I2$ represents a coarser sampling interval and $I1$ represents a finer interval of the same data set. Results shown (a-e) for moored current meters and (f-j) for model grid points in NANLOM2 (a 6 hourly sampled nonassimilative simulation of NLOM). In Figures 11a, 11b, 11c, 11d, and 11e, source denotes the original mooring data, sampled at intervals from 15 min to 3 hours depending on the mooring. All other sampling intervals are given at the top of Figures 11a, 11b, 11c, 11d, 11e, 11f, 11g, 11h, 11i, and 11j. Only the 224 moorings and the 2094302 model grid points for which $0.0025\ \rho\ \overline{|\mathbf{u}_b|^3_{I1}}$ exceeds 1 mW m^{-2} are used.

DANLOM, NANLOM, and POP. In Figures 11c, 11d, and 11e we set $I2$ = 1, 3, and 10 days, the sampling periods of these three simulations, respectively. The daily minus 6 hourly histogram (Figure 11c) looks very similar to the daily minus source histogram (Figure 11b), as expected. The histograms made with $I2$ = 3 and 10 days (Figures 11d and 11e, respectively) become progressively wider, meaning that the $\overline{|\mathbf{u}_b|^3}$ values at individual current meters become less and less reliable as the sampling period increases. Note that the results plotted in Figures 11a, 11b, 11c, 11d, and 11e are dependent on the record lengths, which vary between current meters, as well as on the subsampling period.

[44] In Figures 11f, 11g, 11h, 11i, and 11j, α is calculated from NANLOM2, using $I1$ = 6 hours and $I2$ = 1, 3, 10, 20, and 40 days, respectively. As in the mooring analyses, we

only use model grid points for which $0.0025\ \rho\ \overline{|\mathbf{u}_b|^3_{I1}}$ exceeds 1 mW m^{-2}. There are 2094302 such model grid points. For $I2 = 1$ and 3 days, the histograms of α (Figures 11f and 11g, respectively) are quite narrow, demonstrating that the subsamplings used in DANLOM and NANLOM are adequate for our purposes. For $I2 = 10$ days, the sampling period for POP, the histogram (Figure 11h) has roughly the same width as the histogram of the daily subsampled mooring data (Figures 11b and 11c). The histograms for 20- and 40-day subsampling of NANLOM2 (Figures 11i and 11j, respectively) are of comparable widths to the histograms for 3- and 10-day sampling, respectively, of the current meter data. All of this further suggests that these simulations do not have as much high-frequency variability as the current meters, making the aliasing problem less severe than it is in the current meters for the same sampling interval.

[45] The histograms of both current meter data and model output display approximately similar numbers of negative and positive α values, meaning that when subsampling matters it can either decrease or increase the $\overline{|\mathbf{u}_b|^3}$ estimates. The average over all of the moorings (or model grid points) of $\overline{|\mathbf{u}_b|^3}$ is therefore relatively unaffected. In the analyses shown in Figures 11a, 11b, 11c, 11d, and 11e, the averages over the subsampled ($I2$) mooring data are within 8% or less of the averages computed from the better sampled ($I1$) data. If we use only abyssal moorings the comparison is even closer. In the analyses shown in Figures 11f, 11g, 11h, 11i, and 11j, the area-weighted averages over all of the NANLOM2 grid points of the subsampled $\overline{|\mathbf{u}_b|^3}$ values lie within 3% or less of the area-weighted averages of the 6 hourly values. The latter exercise demonstrates that the $[\overline{D}]$ estimates given in section 5 are not severely affected by the infrequent temporal sampling of the models.

7. Wind-Power Input

[46] To test whether the energy inputs into the models are of the expected magnitude, we calculate the wind-power input for the NANLOM simulation. We use the formula

$$W = \int \boldsymbol{\tau} \cdot \mathbf{u}_g \, dA, \tag{5}$$

where $\boldsymbol{\tau}$ is wind stress and $\mathbf{u}_g$ is the geostrophic velocity at the sea surface, calculated from centered-differencing of the model sea surface height fields. The latitude band 3°S–3°N is excluded from the calculation, since the geostrophic relation is not valid on the equator. The average wind work over year 2002 calculated from NANLOM snapshots put out every 3 days is $W = 0.61$ TW, comparable to but somewhat lower than the 0.75–0.9 TW estimated by *Scott and Xu* [2008] for the wind work poleward of 3°.

8. Summary and Discussion

[47] Computations on the output of three existing global high-resolution simulations strongly suggest that the energy dissipation rate of the oceanic general circulation by quadratic bottom boundary layer drag represents a significant fraction of the ~1 TW wind-power input transformed into geostrophic flows. The range of dissipation estimates over all water depths obtained from the simulations is 0.14–0.65 TW, quite comparable to the 0.21–0.83 TW of dissipation in waters deeper than 3000 m estimated by *Sen et al.* [2008] from observations alone. In addition, the patterns of dissipation estimates obtained from the models are qualitatively similar to those obtained from observations in the paper by *Sen et al.* [2008]. Both the model-based and observationally based maps show dissipation concentrated in strong flows such as the Gulf Stream, Kuroshio, Antarctic Circumpolar Current, etc.

[48] Prior to the computations of dissipation, we compared the time average of the cube of bottom velocities ($\overline{|\mathbf{u}_b|^3}$) computed from the simulations, with $\overline{|\mathbf{u}_b|^3}$ values computed from near-bottom moored current meters. The comparisons focus on $\overline{|\mathbf{u}_b|^3}$ because it is proportional to the dissipation rate. The comparisons indicate that numerical simulations generally have difficulty matching individual current meter records. However, the ratio of the average of the model $\overline{|\mathbf{u}_b|^3}$ values at 274 moored near-bottom current meter sites in the abyssal ocean to the average computed from the current meters themselves is of order one (0.37–0.73) for all three simulations. This suggests that the model estimates of areally integrated dissipation rate should be correct to within an order of magnitude.

[49] Since the ratio just described is less than one in the abyss, and is much less than one in shallow waters for the NLOM simulations, some of our computed dissipation rates are likely to be underestimates. The wind-power input into NANLOM was found to be ~0.15–0.3 TW lower than observational estimates [*Scott and Xu*, 2008], further reinforcing the possibility that some of our computed dissipation rates are likely to be underestimates. On the other hand, there are two reasons to believe that DANLOM in particular may overestimate the dissipation. DANLOM shows dissipation in regions where it is not found in the other models. In addition, the data assimilation methodology used in DANLOM is not energy conserving, such that the data assimilation process constitutes an extra, unphysical energy source for DANLOM.

[50] The estimated dissipation rates in the Southern Ocean represent a substantial fraction of the total dissipation. However, they fall far short of the wind-power input into that region, suggesting that either bottom drag in other regions of the ocean, or mechanisms other than bottom drag acting in the Southern Ocean, balance a substantial fraction of the local input. Similarly, since the lower end of our global dissipation estimates balances only about 15–20% of the global wind-power input, we conclude as we did in the paper by *Sen et al.* [2008] that dissipation mechanisms other than bottom boundary layer drag are also likely to be significant contributors to the global energy budget of the general circulation. In the models utilized here, energy which is not dissipated by bottom drag is dissipated at small horizontal scales, either by eddy viscosity (NLOM), or biharmonic viscosity (POP). The extent to which the transfer of geostrophic energy to smaller scales represents a significant dissipator in the real ocean is an area of active research [e.g., *Müller et al.*, 2005; *Polzin*, 2008]. It is quite possible that small-scale damping operators such as eddy viscosity will ultimately be seen as extremely crude proxies

for the actual physics of such transfers. The generation of internal waves by geostrophic flows over rough topography [e.g., *Naveira-Garabato et al.*, 2004; *Marshall and Naveira-Garabato*, 2008; *Nikurashin*, 2008] is another potentially important dissipation mechanism that is not included even in a crude way in the models utilized in this study.

[51] High-resolution ocean models continue to improve and as they do so the computations performed here will bear repeating. As discussed in this paper, higher resolution in both the vertical and horizontal directions will almost certainly improve the comparison of bottom flows in models to those in observations. Improvements in bottom bathymetry products and in data assimilation schemes, and inclusion of effective parameterizations of other dissipation mechanisms in addition to bottom boundary layer drag, are also likely to have a positive impact in this regard.

[52] **Acknowledgments.** This paper was originally submitted in much shorter form to a different journal. The comments of the reviewers of that paper (Steve Jayne and an anonymous reviewer) convinced us that a more comprehensive paper was in order. The same two reviewers were then asked to review the present paper and continued to provide guidance that led to important improvements. We thank both reviewers for their very substantial contributions to the presentation of this work. Jim Richman and Georges Weatherly are also thanked for useful discussions. B.K.A. acknowledges support from Naval Research Laboratory (NRL) contract N000173-06-2-C003 and National Science Foundation (NSF) grant OCE-0623159. R.B.S. acknowledges support from NSF grant OCE-0526412. The NRL coauthors acknowledge support from the 6.1 project "Global remote littoral forcing via deep water pathways", sponsored by the Office of Naval Research under program element 601153N. J.L.M. acknowledges support from the Office of Naval Research and Office of Science (BER), U.S. Department of Energy, under grant DE-FG02-05ER64119. J.L.M. also acknowledges high-performance computing resources at the Naval Oceanographic Office and the Maui High Performance Computing Center (MHPCC) as part of a DOD High-Performance Computing Grand Challenge grant.

References

Arbic, B. K., and G. R. Flierl (2003), Coherent vortices and kinetic energy ribbons in asymptotic, quasi two-dimensional f-plane turbulence, *Phys. Fluids*, *15*, 2177–2189.

Arbic, B. K., and G. R. Flierl (2004), Baroclinically unstable geostrophic turbulence in the limits of strong and weak bottom Ekman friction: Application to mid-ocean eddies, *J. Phys. Oceanogr.*, *34*, 2257–2273.

Arbic, B. K., and R. B. Scott (2008), On quadratic bottom drag, geostrophic turbulence, and oceanic mesoscale eddies, *J. Phys. Oceanogr.*, *38*, 84–103.

Arbic, B. K., G. R. Flierl, and R. B. Scott (2007), Cascade inequalities for forced-dissipated geostrophic turbulence, *J. Phys. Oceanogr.*, *37*, 1470–1487.

Cessi, P., W. R. Young, and J. A. Polton (2006), Control of large-scale heat transport by small-scale mixing, *J. Phys. Oceanogr.*, *36*, 1877–1894.

Duncan, L. M., H. L. Bryden, and S. A. Cunningham (2003), Friction and mixing in the Faroe Bank Channel overflow, *Oceanol. Acta*, *26*, 473–486.

Egbert, R. D., and R. D. Ray (2003), Semi-diurnal and diurnal tidal dissipation from TOPEX/Poseidon altimetry, *Geophys. Res. Lett.*, *30*(17), 1907, doi:10.1029/2003GL017676.

Ferrari, R., and C. Wunsch (2008), Ocean circulation kinetic energy — Reservoirs, sources, and sinks, *Annu. Rev. Fluid Mech.*, *41*, 253–282.

Fox, D. N., W. J. Teague, C. N. Barron, M. R. Carnes, and C. M. Lee (2002), The modular ocean data assimilation system (MODAS), *J. Atmos. Oceanic Technol.*, *19*, 240–252.

Garner, S. T. (2005), A topographic drag closure built on an analytical base flux, *J. Atmos. Sci.*, *62*, 2302–2315.

Hallberg, R., and P. Rhines (1996), Buoyancy-driven circulation in an ocean basin with isopycnals intersecting the sloping boundary, *J. Phys. Oceanogr.*, *26*, 914–940.

Hellerman, S., and M. Rosenstein (1983), Normal monthly wind stress over the world ocean with error estimates, *J. Phys. Oceanogr.*, *13*, 1093–1104.

Hogan, P. J., and H. E. Hurlburt (2000), Impact of upper ocean-topographical coupling and isopycnal outcropping in Japan/East Sea models with 1/8° to 1/64° resolution, *J. Phys. Oceanogr.*, *30*, 2535–2561.

Huang, R. X., W. Wang, and L. L. Liu (2006), Decadal variability of wind-energy input to the world ocean, *Deep Sea Res., Part II*, *53*, 31–41.

Hurlburt, H. E. (1986), Dynamic transfer of simulated altimeter data into subsurface information by a numerical ocean model, *J. Geophys. Res.*, *91*, 2372–2400.

Hurlburt, H. E., and P. J. Hogan (2000), Impact of 1/8° to 1/64° resolution on Gulf Stream model-data comparisons in basin-scale subtropical Atlantic Ocean models, *Dyn. Atm. Oceans*, *32*, 283–329.

Hurlburt, H. E., and J. D. Thompson (1980), A numerical study of Loop Current intrusions and eddy shedding, *J. Phys. Oceanogr.*, *10*, 1611–1651.

Hurlburt, H. E., and J. D. Thompson (1982), The dynamics of the Loop Current and shed eddies in a numerical model of the Gulf of Mexico, in *Hydrodynamics of Semi-Enclosed Seas*, edited by J. C. J. Nihoul, pp. 243–297, Elsevier, New York.

Hurlburt, H. E., D. N. Fox, and E. J. Metzger (1990), Statistical inference of weakly correlated subthermocline fields from satellite altimeter data, *J. Geophys. Res.*, *95*, 11,375–11,409.

Jakobsson, M., N. Chervis, J. Woodward, B. Coakley, and R. Macnab (2000), A new grid of Arctic bathymetry: A significant resource for scientists and mapmakers, *Eos Trans. AGU*, *81*(9), 89.

Jayne, S. R., and L. C. St. Laurent (2001), Parameterizing tidal dissipation over rough topography, *Geophys. Res. Lett.*, *28*, 811–814.

Jayne, S. R., and R. Tokmakian (1997), Forcing and sampling of ocean general circulation models: Impact of high-frequency motions, *J. Phys. Oceanogr.*, *27*, 1173–1179.

Kalnay, E., et al. (1996), The NCEP/NCAR 40-year reanalysis project, *Bull. Am. Meteorol. Soc.*, *77*, 437–471.

Large, W. G., and S. Pond (1982), Sensible and latent heat flux measurements over the oceans, *J. Phys. Oceanogr.*, *12*, 464–482.

Lythe, M. B., and D. G. Vaughan (2001), BEDMAP: A new ice thickness and subglacial topographic model of Antarctica, *J. Geophys. Res.*, *106*, 11,335–11,351.

Marshall, D. P., and A. C. Naveira-Garabato (2008), A conjecture on the role of bottom-enhanced diapycnal mixing in the parameterization of geostrophic eddies, *J. Phys. Oceanogr.*, *38*, 1607–1613.

Maltrud, M. E., and J. L. McClean (2005), An eddy resolving global 1/10° simulation, *Ocean Modell.*, *8*, 31–54.

McClean, J. L., P.-M. Poulain, J. W. Pelton, and M. E. Maltrud (2002), Eulerian and Lagrangian statistics from surface drifters and a high-resolution POP simulation in the North Atlantic, *J. Phys. Oceanogr.*, *32*, 2472–2491.

Müller, P., J. C. McWilliams, and M. J. Molemaker (2005), Routes to dissipation in the ocean: The 2D/3D turbulence conundrum, in *Marine Turbulence*, edited by H. Z. Baumert, J. Simpson, and J. Sündermann, pp. 397–405, Cambridge Univ. Press, Cambridge, U.K.

Munk, W., and C. Wunsch (1998), Abyssal recipes II: Energetics of tidal and wind mixing, *Deep Sea Res., Part I*, *45*, 1977–2010.

National Oceanic and Atmospheric Administration (1986), ETOPO5 digital relief of the surface of the Earth, *Data Announce. 86–MGG-07*, Natl. Geophys. Data Cent., Boulder, Colo.

Naveira-Garabato, A. C., K. L. Polzin, B. A. King, K. J. Heywood, and M. Visbeck (2004), Widespread intense turbulent mixing in the Southern Ocean, *Science*, *303*, 210–213.

Nikurashin, M. (2008), Radiation and dissipation of internal waves generated by geostrophic motions impinging on small-scale topography, Ph.D. thesis, Mass. Inst. of Technol./Woods Hole Oceanogr. Inst. Joint Program, Cambridge.

Penduff, T., B. Barnier, J.-M. Molines, and G. Madec (2006), On the use of current meter data to assess the realism of ocean model simulations, *Ocean Modell.*, *11*, 399–416.

Polzin, K. L. (2008), Mesoscale eddy-internal wave coupling. Part I: Symmetry, wave capture, and results from the mid-ocean dynamics experiment, *J. Phys. Oceanogr.*, *38*, 2556–2574.

Riviere, P., A. M. Treguier, and P. Klein (2004), Effects of bottom friction on nonlinear equilibration of an oceanic baroclinic jet, *J. Phys. Oceanogr.*, *34*, 416–432.

Rosmond, T. E., J. Teixeira, M. Peng, T. F. Hogan, and R. Pauley (2002), Navy operational global atmospheric prediction system (NOGAPS): Forcing for ocean models, *Oceanography*, *15*, 99–108.

Schmitz, W. J., Jr., and J. D. Thompson (1993), On the effects of horizontal resolution in a limited-area model of the Gulf Stream system, *J. Phys. Oceanogr.*, *23*, 1001–1007.

Scott, R. B. (1999), Mechanical energy flux to the surface geostrophic flow using TOPEX/Poseidon data, *Phys. Chem. Earth*, *24*, 399–402.

Scott, R. B., and Y. Xu (2008), An update on the wind power input to the surface geostrophic flow of the World Ocean, *Deep Sea Res., Part I*, in press.

Sen, A., R. B. Scott, and B. K. Arbic (2008), Global energy dissipation rate of deep-ocean low-frequency flows by quadratic bottom boundary layer drag: Computations from current meter data, *Geophys. Res. Lett.*, *35*, L09606, doi:10.1029/2008GL033407.

Shea, D. J., K. E. Trenberth, and R. W. Reynolds (1990), A global monthly sea surface temperature climatology, *Tech. Note NCAR/TN-345*, Natl. Cent. for Atmos. Res., Boulder, Colo.

Shriver, J. F., H. E. Hurlburt, O. M. Smedstad, A. J. Wallcraft, and R. C. Rhodes (2007), 1/32° real-time global ocean prediction and value-added over 1/16° resolution, *J. Mar. Syst.*, *65*, 3–26.

Smith, K. S., G. Boccaletti, C. C. Henning, I. N. Marinov, C. Y. Tam, I. M. Held, and G. K. Vallis (2002), Turbulent diffusion in the geostrophic inverse cascade, *J. Fluid Mech.*, *469*, 13–48.

Smith, R. D., M. E. Maltrud, F. Bryan, and M. W. Hecht (2000), Numerical simulation of the North Atlantic Ocean at 1/10°, *J. Phys. Oceanogr.*, *30*, 1532–1561.

Smith, W. H. F., and D. T. Sandwell (1997), Global seafloor topography from satellite altimetry and ship depth soundings, *Science*, *277*, 1956–1962.

Steele, M., R. Morley, and W. Ermold (2001), PHC: A global ocean hydrography with a high-quality Arctic Ocean, *J. Clim.*, *14*, 2079–2087.

Taylor, G. I. (1919), Tidal friction in the Irish Sea, *Philos. Trans. R. Soc. London, Ser. A*, *220*, 1–33.

Thompson, A. F., and W. R. Young (2006), Scaling baroclinic eddy fluxes: Vortices and energy balance, *J. Phys. Oceanogr.*, *36*, 720–738.

Thompson, A. F., and W. R. Young (2007), Baroclinic eddy heat fluxes: Zonal flows and energy balance, *J. Atmos. Sci.*, *64*, 3214–3231.

Thompson, J. D., and W. J. Schmitz Jr. (1989), A limited-area model of the Gulf Stream: Design, initial experiments, and model-data intercomparison, *J. Phys. Oceanogr.*, *19*, 791–814.

Trowbridge, J. R., and S. J. Lentz (1998), Dynamics of the bottom boundary layer on the Northern California Shelf, *J. Phys. Oceanogr.*, *28*, 2075–2093.

Wallcraft, A. J., A. B. Kara, H. E. Hurlburt, and P. A. Rochford (2003), The NRL Layered Ocean Model (NLOM) with an embedded mixed layer sub-model: Formulation and tuning, *J. Atmos. Oceanic Technol.*, *20*, 1601–1615.

Wallcraft, A. J., A. B. Kara, and H. E. Hurlburt (2005), Convergence of Laplacian diffusion versus resolution of an ocean model, *Geophys. Res. Lett.*, *32*, L07604, doi:10.1029/2005GL022514.

Weatherly, G. L. (1984), An estimate of bottom frictional dissipation by Gulf Stream fluctuations, *J. Mar. Res.*, *42*, 289–301.

Weatherly, G. L., and P. J. Martin (1978), On the structure and dynamics of the oceanic bottom boundary layer, *J. Phys. Oceanogr.*, *8*, 557–570.

Wunsch, C. (1997), The vertical partition of oceanic horizontal kinetic energy, *J. Phys. Oceanogr.*, *27*, 1770–1794.

Wunsch, C. (1998), The work done by the wind on the oceanic general circulation, *J. Phys. Oceanogr.*, *28*, 2332–2340.

Wunsch, C., and R. Ferrari (2004), Vertical mixing, energy, and the general circulation of the oceans, *Annu. Rev. Fluid Mech.*, *36*, 281–314.

B. K. Arbic, Department of Oceanography, Florida State University, Tallahassee, FL 32306-2840, USA. (barbic@fsu.edu)

P. J. Hogan, H. E. Hurlburt, E. J. Metzger, J. F. Shriver, and A. J. Wallcraft, Oceanography Division, Naval Research Laboratory, Stennis Space Center, MS 39529, USA.

J. L. McClean, Scripps Institution of Oceanography, University of California, San Diego, La Jolla, CA 92093, USA.

R. B. Scott, Institute for Geophysics, Jackson School of Geosciences, University of Texas at Austin, Austin, TX 78758, USA.

A. Sen, Department of Applied and Computational Math, California Institute of Technology, Pasadena, CA 91125, USA.

O. M. Smedstad, Planning Systems, Inc., Stennis Space Center, MS 39529, USA.